CHEMISTRY OF MATERIALS

pubs.acs.org/cm

Article

On the Phase Stability of Chalcogenide Perovskites

Alexander Jess, Ruiquan Yang, and Charles J. Hages*

Cite This: *Chem. Mater.* 2022, 34, 6894–6901

Read Online

ACCESS | Metrics & More | Article Recommendations | Supporting Information

ABSTRACT: Chalcogenide perovskites have gained recent research attention as a promising semiconductor for photovoltaic and optoelectronic applications. In addition to the challenges that surround the synthesis and processing of these materials into devices, their phase stability in perovskite structures is an open research question. Reported syntheses presently lack clear phase stability criteria. In this work, we present a compelling phase stability analysis of sulfide ABS_3 and selenide $ABSe_3$ compounds on the basis of ionic radii and electronegativity arguments. This analysis is used to screen potential materials of interest as well as motivate further experimental research into several new perovskite compositions.

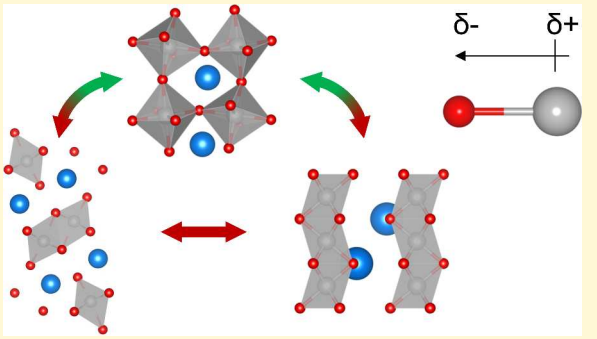

Chalcogenide perovskites—eponymously named for containing S, Se, or Te as the anion—are an emerging frontier in Pb-free, inorganic perovskites with high stability and promising optoelectronic properties. This class of materials has recently gained interest as semiconductors for photovoltaic (PV) and optoelectronic applications.[1−11] While a number of promising compounds have been identified from theoretical simulations,[2,12,13] there is a significant lack of relevant experimental syntheses reported for chalcogenide perovskites. Furthermore, synthesized compounds historically lack clear phase stability criteria to guide experimental work.

Chalcogenide perovskites have the basic perovskite chemical formula ABX_3, where X is a chalcogen anion (S^{2-}, Se^{2-}, Te^{2-}). Constituent elements for commonly considered A-site and B-site cations result in a large material space exceeding 1800 compounds, shown for $A^{2+}B^{4+}S_3$ and $A^{2+}B^{4+}Se_3$ in Tables 1a and 1b, respectively. The use of chalcogenide anions follows logically from the prevalence of oxide perovskites, both in research and as one of the most common minerals on earth; 90% of metal elements are stable in an oxide perovskite phase.[14] While oxide perovskites have several applications as electronic materials,[15−21] their band gap is generally too large to interact with visible and IR light. This is a result of the large electronegativity of oxygen yielding localized orbitals for the valence and conduction bands.[22] However, the reduced electronegativity of chalcogenides relative to oxygen results in increased covalent bonding in chalcogenide perovskites. This reduces the band gap to an ideal range for optoelectronic emitters and absorbers,[20,23] among other favorable optoelectronic properties.[4,8,24−26] However, this electronegativity difference can also result in a shift in the phase stability of chalcogenide relative to oxide perovskites for a given choice of cations.

The structure of ABX_3 compounds has a significant impact on the resulting properties of the material. The ideal perovskite crystal structure is illustrated in Figure 1a for $SrTiO_3$. It can be described as a 3D-network of corner-sharing BX_6 octahedra held together by the A-site cation occupying the cuboctahedra cavities.[27] However, this ideal structure only forms for a narrow range of cation sizes or synthesis conditions. In fact, perovskites have a rich phase complexity forming cubic, tetragonal, orthorhombic, trigonal, and monoclinic phases depending on the tilting and rotation of the BX_6 octahedra in the crystal lattice.[28−30] One of the most common perovskite polytypes, when the A-site cation is too small to fit into the B-site cation interstices, is the "distorted perovskite" structure illustrated for $GdFeO_3$ in Figure 1b. In both ideal and distorted perovskite structures, the corner-sharing octahedra are essential to produce direct-band gap semiconductors with high absorption in the relevant energy range for optoelectronic applications, with desirable isotropic and high electron mobility. This is a result of dispersive electronic bands due to the high symmetry and electron configuration of the B-site cation and B−X antibonding.[29,31,32]

When a relatively large A-site cation is used in the ABX_3 structure, lattice strain is relieved by the formation of a hexagonal perovskite polytype,[29,33] resulting in BX_6 octahedra in a face-sharing rather than corner-sharing configuration. This is illustrated for $BiNiO_3$ in Figure 1c, which has continuous

Received: April 28, 2022
Revised: July 6, 2022
Published: July 18, 2022

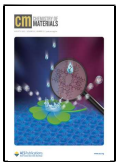

https://doi.org/10.1021/acs.chemmater.2c01289
Chem. Mater. 2022, 34, 6894−6901

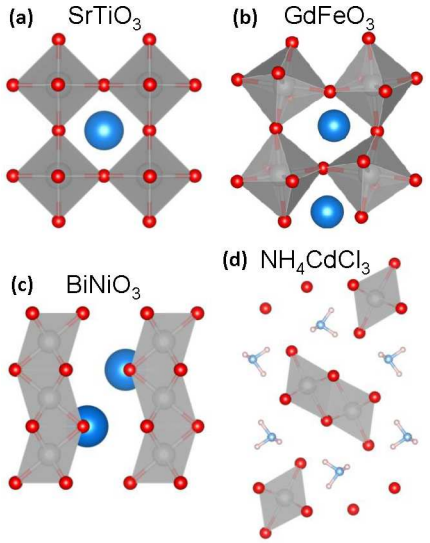

Figure 1. Common structural polytypes for ABX_3: (a) ideal cubic perovskite, (b) distorted perovskite, (c) hexagonal perovskite polytype, and (d) nonperovskite needle-like phase. The A-site cation is shown as blue, the B-site cation as gray, and the anion as red for the different materials.

1D-chains of all face-sharing octahedra. A range of hexagonal perovskite polytypes can be formed with a mixture of corner- and face-sharing (see $BaRuO_3$, for example).[29,34] As the B-site connectivity increases in these hexagonal polytypes, dramatic changes in the optoelectronic properties occur. This includes 1D quantum confinement effects, a significant widening or reduction of the band gap, and an anisotropic flattening of the band dispersion reducing carrier mobility in different crystal directions.[12,29,35−37] Such structures demonstrate interesting optoelectronic properties (e.g., large birefringence, nonlinearity, tunable IR bandgap, ion conductivity),[5,7,38,39] though have generally not been applied to PV. When a relatively small A-site cation is used in the ABX_3 structure, octahedral connectivity can be disrupted, resulting in a "needle-like" structure shown for NH_4CdCl_3 in Figure 1d. This structure has distinctly different and generally undesirable optoelectronic properties and is not considered to be perovskite here.[31,40] ABX_3 compounds can also form into so-called "misfit layer compounds" which can demonstrate interesting superconductivity and intercalation properties.[41,42] It should be noted that there are a number of other interesting dimensionally reduced, defect, hexagonal polytype, double perovskite, and antiperovskite structures which exhibit perovskite-type connectivity and optoelectronic behavior,[43−45] though they deviate from the ABX_3 stoichiometry considered herein.

The synthesis of ABX_3 chalcogenides has been reported a number of times over the past 60 years in a variety of stable phases. For $A^{2+}B^{4+}X_3$, initial reports focused on alkali earth metal A-site cations (Ba, Sr, Ca) with Group IVA B-site cations (Hf, Zr, Ti).[6,7,10,11,23,38,46−73] Shortly after, Pb(II)/Sn(II) and Pb(IV)/Sn(IV) were introduced for the A-site and B-site cations, respectively.[42,74−84] B-site Group V elements (Ta, Nb, and V)[52,53,56,67,85−87] as well as A-site Eu[46,88] and Cu[89] were subsequently included. Compounds with radioactive A-site U/Th have been reported predominately in an alternative $A^{4+}B^{2+}X_3$ phase,[90,91] with the exception of $BaU(S,Se)_3$ with B-site U since $U^{4+} < Ba^{2+}$ w.r.t ionic radius.[92,93] A summary of reported experimental syntheses (whose phases are indicated by shading in various colors) are shown in Tables 1a and 1b for sulfide and selenide $A^{2+}B^{4+}X_3$ chalcogenides, respectively. Of the synthesized compounds, 10 distorted perovskites ($GdFeO_3$-type) are shown in green, 11 hexagonal perovskite polytypes ($BiNiO_3$-type) are shown in purple, 10 needle-like (NH_4CdCl_3-type) phases are shown in yellow, and 11 other ABX_3 nonperovskite phases—generally misfit layer compounds[41]—are shown in red. Several other studies have also focused on phase transitions that occur for high-pressure syntheses (not included in our phase stability analyses).[54,80,81,94] Following sparse early work, an increase in publications occurred in 2014 with a marked interest in optoelectronic behavior. As an example, Sun et al.[2] followed by others have theoretically and/or experimentally identified several chalcogenide perovskites as promising candidates for PV from bandgap, absorption, and carrier mobility screening,[2,12,13,95,96] which is indicated in bold red text in Tables 1 and 2. In this work, we mainly consider the described $A^{2+}B^{4+}X_3$ compounds which have been the dominate focus for semiconducting and PV applications. However, a number of additional $A^{3+}B^{3+}X_3$ compounds utilizing lanthanide, Y, and Sc cations have also been experimentally reported in a variety of phases;[1,96] their analysis is included in the Supporting Information along with other data used for calculations throughout.

As the optoelectronic properties have a strong dependence on the crystal structure, it is critical to understand stable phase formation in these ABX_3 compounds. To predict stable phase formation, the Goldschmidt tolerance factor[97] $t = (r_A + r_X)/(\sqrt{2}(r_B + r_X))$ is commonly used, where r_A, r_B, and r_X are the corresponding ionic radii[98] for the A-site, B-site, and chalcogen atoms in the crystal lattice. For ABO_3 oxide perovskites, $t > 1.06$ predicts hexagonal polytypes ($BiNiO_3$-type), $1.06 > t > 0.83$ predicts ideal and distorted ($GdFeO_3$-type) perovskite phases, and $t < 0.83$ predicts nonperovskite phases, in general.[30,99] This tolerance factor is computed for sulfide $A^{2+}B^{4+}S_3$ and selenide $A^{2+}B^{4+}Se_3$ compounds in Tables 1a and 1b, respectively, along with an indication of the historical border for each stable phase region. ***Here we see the traditional Goldschmidt tolerance factor bounds fail to predict the resulting stable phase.*** Furthermore, ***there is no correlation between the reported stable phase and tolerance factor (i.e., cation radius).*** The fundamental failure of tolerance factors based on ionic radius for ABX_3 is most apparent when observing Pb(II) and Sn(II) as A-site cations as their resulting stable phases do not correlate with ionic radius. This lack of correlation is also observed when using updated prediction factors with various modifications based on oxide and halide perovskites, since these alternative tolerance factors similarly trend with ionic radius (see SI).[99,100] The failure of structural prediction techniques makes directing experimental work on these new compounds challenging.

To reconcile this, we propose a modified tolerance factor which accounts for electronegativity, based on similar arguments made by Pearson[101] and Brehm et al.,[102] which we find predicts stable phase formation quite well for ABX_3 phases when compared to known experimental data. One of the main chemical differences in chalcogenide relative to oxide perovskites is the drop in electronegativity from oxygen to sulfur and selenium. This contributes to the increased covalent bonding in chalcogenides relative to ionic bonding in the oxide perovskites. As a result, bond lengths $(r_A + r_X)$ and $(r_B + r_X)$ used in calculating the Goldschmidt tolerance factor—based

https://doi.org/10.1021/acs.chemmater.2c01289
Chem. Mater. 2022, 34, 6894−6901

Table 1. Goldschmidt Tolerance Factor for (a) $A^{2+}B^{4+}S_3$ Sulfides and (b) $A^{2+}B^{4+}Se_3$ Selenides[a]

(a) ABS_3 sulfides.

A^{2+}-Site \ B^{4+}-site	Si	Ge	V	Rh	Ti	Ru	Mo	Ta	Nb	Sn	Hf	Zr	Tb	Pb	Pt	Ce	U
Ba	1.09	1.03	**1.01**	1.00	**1.00**	0.99	0.98	**0.97**	**0.97**	0.96	**0.96**	**0.95**	0.94	0.93	0.92	0.90	**0.89**
Eu	1.04	0.98	0.96	0.95	0.95	0.95	0.93	0.92	0.92	0.92	**0.91**	**0.91**	0.89	0.89	0.88	0.86	0.85
Pb	1.04	0.98	**0.96**	0.95	**0.95**	0.94	0.93	**0.92**	**0.92**	**0.92**	**0.91**	**0.91**	0.89	0.89	0.88	0.86	0.85
Sr	1.04	0.98	0.96	0.95	**0.95**	0.94	0.93	0.92	0.92	**0.92**	**0.91**	**0.91**	0.89	0.89	0.88	0.86	0.85
Ca	1.00	0.95	0.93	0.92	**0.92**	0.91	0.90	0.89	0.89	**0.89**	**0.88**	**0.88**	0.86	0.86	0.85	0.83	0.82
Sn	1.00	0.95	**0.93**	0.92	**0.92**	0.91	0.90	**0.89**	**0.89**	**0.89**	**0.88**	**0.88**	0.86	0.86	0.85	0.83	0.82
Cd	0.99	0.94	0.92	0.91	0.91	0.91	0.89	0.88	0.88	0.88	0.87	0.87	0.86	0.85	0.84	0.82	0.82
Cu	0.96	0.91	0.89	0.88	0.88	0.88	0.87	**0.86**	0.86	0.85	0.85	0.84	0.83	0.82	0.82	0.80	0.79
Mg	0.96	0.91	0.89	0.88	0.88	0.87	0.86	0.85	0.85	0.85	0.84	0.84	0.83	0.82	0.81	0.79	0.79
Zn	0.96	0.90	0.89	0.88	0.88	0.87	0.86	0.85	0.85	0.85	0.84	0.84	0.82	0.82	0.81	0.79	0.78
Ge	0.87	0.82	0.80	0.80	0.80	0.79	0.78	0.77	0.77	0.77	0.76	0.76	0.75	0.74	0.74	0.72	0.71

Hexagonal border (>1.06)

Non-perovskite border (<0.83)

(b) $ABSe_3$ selenides.

A^{2+}-Site \ B^{4+}-site	Si	Ge	V	Rh	Ti	Ru	Mo	Ta	Nb	Sn	Hf	Zr	Tb	Pb	Pt	Ce	U
Ba	1.07	1.01	**0.99**	0.98	**0.98**	0.98	0.97	**0.95**	**0.95**	0.95	**0.94**	**0.94**	0.93	0.92	0.91	0.89	**0.88**
Eu	1.02	0.97	0.95	0.94	0.94	0.93	0.92	0.91	0.91	0.91	0.90	**0.90**	0.89	0.88	0.87	0.85	0.85
Pb	1.02	0.96	0.94	0.94	0.94	0.93	0.92	0.91	**0.91**	0.91	0.90	0.90	0.88	0.88	0.87	0.85	0.84
Sr	1.02	0.96	0.94	0.94	**0.94**	0.93	0.92	0.91	0.91	**0.91**	**0.90**	**0.90**	0.88	0.88	0.87	0.85	0.84
Ca	0.99	0.94	0.92	0.91	0.91	0.90	0.89	0.88	0.88	0.88	**0.87**	**0.87**	0.86	0.85	0.84	0.82	0.82
Sn	0.98	0.93	**0.91**	0.91	0.91	0.90	0.89	0.88	**0.88**	0.88	0.87	**0.87**	0.85	0.85	0.84	0.82	0.82
Cd	0.98	0.93	0.91	0.90	0.90	0.89	0.88	0.87	0.87	0.87	0.86	0.86	0.85	0.84	0.84	0.82	0.81
Cu	0.95	0.90	0.88	0.87	0.87	0.87	0.86	0.85	0.85	0.84	0.84	0.84	0.82	0.82	0.81	0.79	0.79
Mg	0.94	0.90	0.88	0.87	0.87	0.86	0.85	0.85	0.85	0.84	0.84	0.83	0.82	0.82	0.81	0.79	0.78
Zn	0.94	0.89	0.88	0.87	0.87	0.86	0.85	0.84	0.84	0.84	0.83	0.83	0.82	0.81	0.81	0.79	0.78
Ge	0.86	0.81	0.80	0.79	0.79	0.79	0.78	0.77	0.77	0.77	0.76	0.76	0.75	0.74	0.74	0.72	0.71

Hexagonal border (>1.06)

Non-perovskite border (<0.83)

Increasing Ionic Radius

Dist. Perovskite ($GdFeO_3$-type)
Hexagonal Polytype ($BiNiO_3$-type)
Needle-like (NH_4CdCl_3-type)
Other non-perovskite

Experimentally Synthesized compounds

[a]The historical borders for the formation of hexagonal polytype and nonperovskite phases are indicated. Cations are arranged by increasing ionic radius vertically and right. The highlighted cells are experimentally reported phases while those with red text are phases theoretically predicted as promising candidates for PV.

on ionic radii reported by Shannon[98]—no longer accurately represent the bond lengths for the ABX_3 compounds. Similar arguments have been made regarding covalency in halide perovskites.[98,99,103] One can also hypothesize that electronegativity—and thus the ionic or covalent bond nature—is critical for structural prediction as Sn(II) and Pb(II) as A-site cations (with relatively high electronegativity) appear to be responsible for several experimental phases which do not correlate with ionic radii. Therefore, a modified tolerance factor $t^\star$ is proposed where the cation−anion bond lengths in the Goldschmidt tolerance factor are modified by the relative change in cation−anion electronegativity difference $\Delta\chi$ relative to oxygen, following:

$$t^\star = \frac{\frac{\Delta\chi_{(A-X)}}{\Delta\chi_{(A-O)}}(r_A + r_X)}{\sqrt{2}\frac{\Delta\chi_{(B-X)}}{\Delta\chi_{(B-O)}}(r_B + r_X)} \quad (1)$$

This new tolerance factor reduces to the Goldschmidt tolerance factor for oxide perovskites. Computed values based on $t^\star$ are shown in Tables 2a and 2b for sulfide and selenide $A^{2+}B^{4+}X_3$ compounds, respectively. In contrast to the traditional Goldschmidt tolerance factor, here we find several key improvements. First, there is now a clear demarcation between the various phases found experimentally, with the new tolerance factor now illustrating the expected clustering of similar phases. Second, there is good agreement with the predicted stable phase boundary regions. The bounds for hexagonal polytype formation ($t^\star \gtrsim 1.06$) are now similar to the bounds found for the traditional Goldschmidt tolerance factor t used for oxide perovskites. Uncertainty in this bound due to missing data from yet-to-be synthesized compounds is reflected by the dashed lines in Tables 2a and 2b. In contrast, we find the lower bound for nonperovskite phase formation increases from ABO_3 ($t < 0.83$) to ABS_3 ($t^\star < (0.90–0.94)$) to $ABSe_3$ ($t^\star < 1.01$), which reduces the stable region for the desired corner-sharing perovskite phase successively. The relatively high electronegativity of Sn(II) and Pb(II) result in a reduction in the new tolerance factor for $SnBX_3$ and $PbBX_3$ compounds, which now accurately predicts a low $t^\star$ and their

https://doi.org/10.1021/acs.chemmater.2c01289
Chem. Mater. 2022, 34, 6894−6901

Table 2. *New* Tolerance Factor $t^{\star}$ for (a) $A^{2+}B^{4+}S_3$ Sulfides and (b) $A^{2+}B^{4+}Se_3$ Selenides[a]

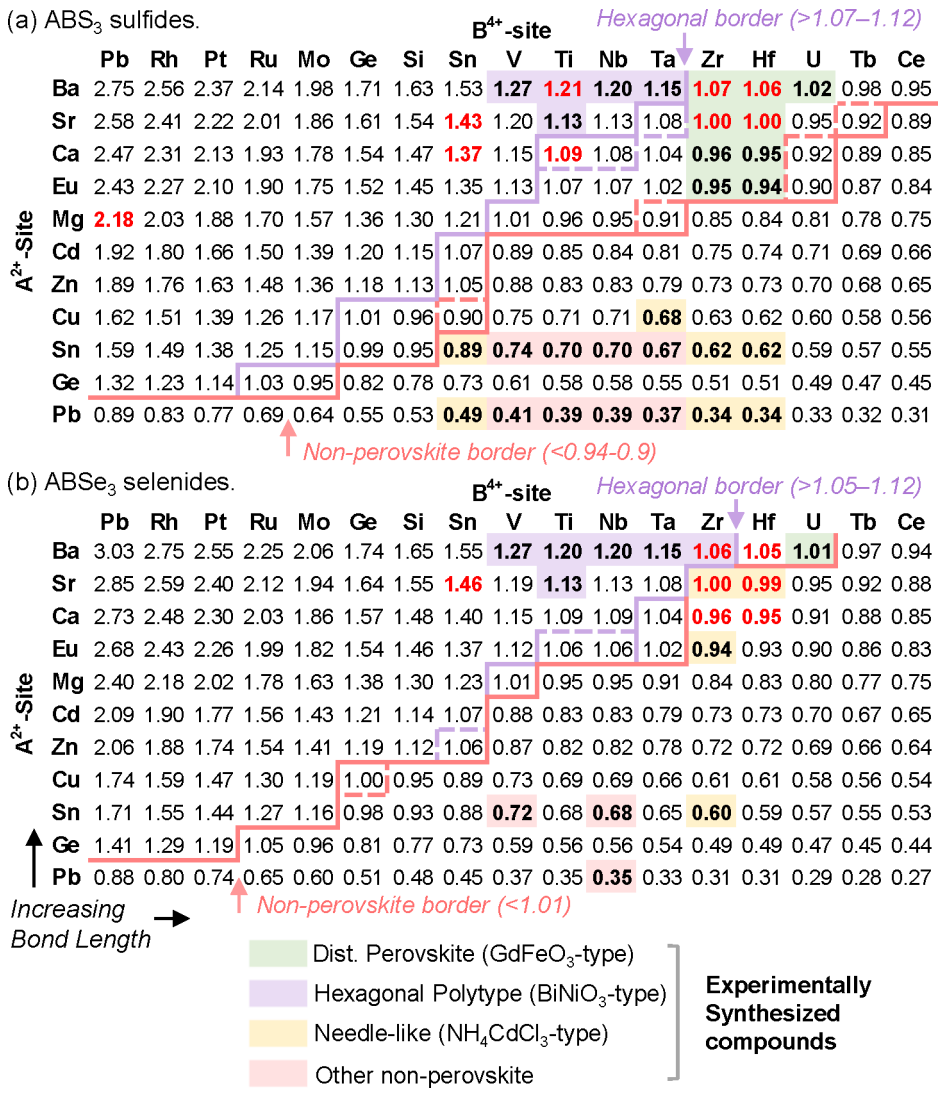

[a]The predicted borders based on experimental data for the formation of hexagonal polytype and nonperovskite phases are indicated. Cations are arranged by increasing bond length vertically and right, accounting for electronegativity following eq 1. The highlighted cells are experimentally reported phases while those with red text are phases theoretically predicted as promising candidates for PV.

resulting nonperovskite phases found experimentally. Accounting for electronegativity difference, we see a general increase in $t^{\star}$ for the chalcogenides relative to oxide perovskites for a given A- and B-site cation. The stability of new compounds as perovskites toward the left side of Table 2 is yet unclear as a low octahedral factor[103] may be important, though further experimental data is needed to understand the bounds on this factor for ABX_3 in light of the increased covalent bonding in these materials. Analysis for $A^{3+}B^{3+}X_3$ compounds is shown in the SI, with similar conclusions observed. Also, analysis of $ABTe_3$ and $A^{1+}B^{5+}X_3$ compounds can be found in the SI, though no experimental phases are known for validation at this time.

Accounting for electronegativity in predicting stable phase formation is not without precedent. Covalent atomic sizes and electronegativity were discussed by Pearson in 1962 in relation to semiconductors.[101] In 1984, Pettifor developed structural field maps to group phases based on their Mendeleev number, which to a large extent reflects their electronegativity.[104] The expected clustering of like phases we observe following $t^{\star}$ can also be achieved if the Goldschmidt tolerance factor is computed on the basis of single-bond covalent radii or ranked according to a Pettifor factor,[102] as these approaches have a similar basis in modifying the A−X and B−X bond lengths. However, inspection of the electronegativity difference between constituent atoms in these bonds for ABX_3 suggests predominately polar covalent bonding; therefore, in $t^{\star}$ we prefer to weight the ionic bond lengths by the electronegativity difference relative to oxygen rather than utilize the purely covalent radii or Pettifor factor (electronegativity) alone. More recently, Brehm et al.[102] have proposed a modified tolerance factor t' for predicting the structure of ABS_3 compounds on the basis of a similar electronegativity difference relative to oxygen for the A−X bond length. In contrast to their work, we consider covalent bonding for both the A−X and B−X bond lengths, as supported by density functional theory on $BaZrS_3$.[20] Accordingly, the tolerance factor herein correlates to the traditional bounds for predicting phase formation (e.g., $BaZrS_3$ has $t' = 0.63$ forming the distorted perovskite phase, while $t^{\star}$ proposed here is in good agreement with the traditional

https://doi.org/10.1021/acs.chemmater.2c01289
Chem. Mater. 2022, 34, 6894−6901

Goldschmidt tolerance factor predicting this phase around $t^{\star}$ = 1.07). Additionally, simulated structures via DFT to identify ground states based on polymorph energy ordering were used to validate their structural prediction factor for a select number of cations. However, many of the identified ground state phases do not agree with experimental phases previously reported; only a single material $BaZrS_3$ is predicted to form the distorted perovskite structure (for $T > 90$ K). In contrast, we consider a comprehensive database of experimentally reported structures—including those for $ABSe_3$. Nonetheless, their work is important in developing our analysis.

Several interesting conclusions can be drawn from the structural predictions resulting from analysis of $t^{\star}$ for ABX_3 materials. First, several sulfide perovskite compounds identified from theory as promising PV materials (highlighted in red text in Table 2a) are not expected to form in the desirable perovskite phase. A notable exception is $BaZrS_3$, which unsurprisingly is the most studied chalcogenide perovskite in recent literature. Alternatively, $CaTiS_3$ is on the border of stable phase formation as a perovskite and warrants further experimental verification. Second, as phases not indicated in bold red cannot be ruled out as desirable semiconductor materials, several sulfide compounds predicted in or near the stable region for perovskite phase formation warrant further experimental demonstration and screening of optoelectronic properties (e.g., $Ba(Tb,Ce)S_3$, $Sr(Ta,Tb)S_3$, $Ca(Nb,Ta)S_3$, and $Eu(Ti,Nb,Ta)S_3$, $Mg(V,Ti,Nb,Ta)S_3$, $(Cd,Zn)SnS_3$, $Cu(Ge,Si,Sn)S_3$, $Sn(Ge,Si)S_3$, $Ge(Ru,Mo)S_3$). Third, inspection of Table 2b indicates that perovskite $ABSe_3$ materials in particular have a narrow predicted stability region. Several compounds warrant further experimental demonstration (e.g., $CaTaSe_3$, $Eu(Ti,Nb,Ta)Se_3$,$MgVSe_3$, $ZnSnSe_3$, and $CuGeSe_3$), including $BaHfSe_3$ which is predicted to have desirable optoelectronic properties for PV. Interesting $A^{3+}B^{3+}X_3$ and $ABTe_3$ phases can also be found from this analysis (see SI). As many ABX_3 compounds of interest lie outside the predicted stable region for perovskite phase formation, alternative synthetic strategies should be considered for phase stabilization; this includes exploring kinetic growth conditions, the role of stoichiometry, and nanomaterial/solution-based growth (i.e., phase stabilization via surface energy). Additionally, cation alloying may be a useful tool to expand these predicted phase boundaries. Finally, while the preceding discussion is generally based around identifying perovskite structures, such analysis is also useful to identify potential compounds in alternative phases for other interesting applications.

In conclusion, we have presented a modified tolerance factor for chalcogenide perovskites which accounts for the expected variations in the bond lengths of constituent atoms in the ABX_3 structure due to electronegativity differences relative to oxide perovskites. Resulting structural predictions are in good agreement with experimentally reported ABS_3 and $ABSe_3$ phases. Screening potential semiconductor PV or optoelectronic materials following this analysis is a useful tool to identify undesirable phases as well as motivate further experimental research into several unrealized perovskite materials.

METHODS

The calculation of tolerance factors reported in this work uses revised effective ionic radii values for r_A, r_B, and r_X based on Shannon,[98] modified by Pauling electronegativity values of the constituent elements. Input data used for these calculations can be found in the Supporting Information.

ASSOCIATED CONTENT

Supporting Information

The Supporting Information is available free of charge at https://pubs.acs.org/doi/10.1021/acs.chemmater.2c01289.

Data used for calculations, additional experimental data and/or theoretical analysis for $A^{3+}B^{3+}X_3$ and $A^{1+}B^{5+}X_3$, analysis for $ABTe_3$, and comparison to alternative tolerance factors (PDF)

AUTHOR INFORMATION

Corresponding Author

Charles J. Hages − *Department of Chemical Engineering, University of Florida, Gainesville, Florida 32611, United States;* orcid.org/0000-0003-4054-1218; Email: c.hages@ufl.edu

Authors

Alexander Jess − *Department of Chemical Engineering, University of Florida, Gainesville, Florida 32611, United States*

Ruiquan Yang − *Department of Chemical Engineering, University of Florida, Gainesville, Florida 32611, United States*

Complete contact information is available at: https://pubs.acs.org/10.1021/acs.chemmater.2c01289

Notes

The authors declare no competing financial interest.

ACKNOWLEDGMENTS

C.J.H. would like to acknowledge financial support from the SSMC program at the National Science Foundation (DMR-2044859).

REFERENCES

(1) Sopiha, K. V.; Comparotto, C.; Márquez, J. A.; Scragg, J. J. S. Chalcogenide Perovskites: Tantalizing Prospects, Challenging Materials. *Advanced Optical Materials* **2022**, *10*, 2101704.

(2) Sun, Y.-Y.; Agiorgousis, M. L.; Zhang, P.; Zhang, S. Chalcogenide Perovskites for Photovoltaics. *Nano Lett.* **2015**, *15*, 581−585.

(3) Buffiere, M.; Dhawale, D. S.; El-Mellouhi, F. Chalcogenide Materials and Derivatives for Photovoltaic Applications. *Energy Technology* **2019**, *7*, 1900819.

(4) Swarnkar, A.; Mir, W. J.; Chakraborty, R.; Jagadeeswararao, M.; Sheikh, T.; Nag, A. Are Chalcogenide Perovskites an Emerging Class of Semiconductors for Optoelectronic Properties and Solar Cell? *Chem. Mater.* **2019**, *31*, 565−575.

(5) Jaramillo, R.; Ravichandran, J. In praise and in search of highly-polarizable semiconductors: Technological promise and discovery strategies. *APL Materials* **2019**, *7*, 100902.

(6) Comparotto, C.; Davydova, A.; Ericson, T.; Riekehr, L.; Moro, M. V.; Kubart, T.; Scragg, J. Chalcogenide Perovskite $BaZrS_3$: Thin Film Growth by Sputtering and Rapid Thermal Processing. *ACS Applied Energy Materials* **2020**, *3*, 2762−2770.

(7) Wu, J.; Cong, X.; Niu, S.; Liu, F.; Zhao, H.; Du, Z.; Ravichandran, J.; Tan, P. H.; Wang, H. Linear Dichroism Conversion in Quasi-1D Perovskite Chalcogenide. *Adv. Mater.* **2019**, *31*, 1902118.

(8) Osei-Agyemang, E.; Balasubramanian, G. Understanding the Extremely Poor Lattice Thermal Transport in Chalcogenide Perovskite $BaZrS_3$. *ACS Applied Energy Materials* **2020**, *3*, 1139−1144.

(9) Vonrüti, N.; Aschauer, U. Band-gap engineering in $AB(O_xS_{1-x})_3$ perovskite oxysulfides: A route to strongly polar materials for photocatalytic water splitting. *Journal of Materials Chemistry A* **2019**, *7*, 15741−15748.
(10) Niu, S.; Milam-Guerrero, J.; Zhou, Y.; Ye, K.; Zhao, B.; Melot, B. C.; Ravichandran, J. Thermal stability study of transition metal perovskite sulfides. *J. Mater. Res.* **2018**, *33*, 4135−4143.
(11) Niu, S.; et al. Giant optical anisotropy in a quasi-one-dimensional crystal. *Nat. Photonics* **2018**, *12*, 392−396.
(12) Huo, Z.; Wei, S.-H.; Yin, W.-J. High-throughput screening of chalcogenide single perovskites by first-principles calculations for photovoltaics. *J. Phys. D: Appl. Phys.* **2018**, *51*, 474003.
(13) Ju, M.-G.; Dai, J.; Ma, L.; Zeng, X. C. Perovskite Chalcogenides with Optimal Bandgap and Desired Optical Absorption for Photovoltaic Devices. *Adv. Energy Mater.* **2017**, *7*, 1700216.
(14) Theofylaktos, L.; Kosmatos, K. O.; Giannakaki, E.; Kourti, H.; Deligiannis, D.; Konstantakou, M.; Stergiopoulos, T. Perovskites with d-block metals for solar energy applications. *Dalton Transactions* **2019**, *48*, 9516−9537.
(15) Grabowska, E. Selected perovskite oxides: Characterization, preparation and photocatalytic properties-A review. *Applied Catalysis B: Environmental* **2016**, *186*, 97−126.
(16) Huang, K.; Tichy, R. S.; Goodenough, J. B. Superior Perovskite Oxide-Ion Conductor; Strontium- and Magnesium-Doped $LaGaO_3$: I, Phase Relationships and Electrical Properties. *J. Am. Ceram. Soc.* **1998**, *81*, 2565−2575.
(17) Shin, S. S.; Yeom, E. J.; Yang, W. S.; Hur, S.; Kim, M. G.; Im, J.; Seo, J.; Noh, J. H.; Seok, S. I. Colloidally prepared La-doped $BaSnO_3$ electrodes for efficient, photostable perovskite solar cells. *Science* **2017**, *356*, 167−171.
(18) Cohen, R. E. Origin of ferroelectricity in perovskite oxides. *Nature* **1992**, *358*, 136−138.
(19) Maeno, Y.; Hashimoto, H.; Yoshida, K.; Nishizaki, S.; Fujita, T.; Bednorz, J. G.; Lichtenberg, F. Superconductivity in a layered perovskite without copper. *Nature* **1994**, *372*, 532−534.
(20) Bennett, J. W.; Grinberg, I.; Rappe, A. M. Effect of substituting of S for O: The sulfide perovskite $BaZrS_3$ investigated with density functional theory. *Physical Review B - Condensed Matter and Materials Physics* **2009**, *79*, 235115.
(21) Homes, C. C.; Vogt, T.; Shapiro, S. M.; Wakimoto, S.; Ramirez, A. P. Optical Response of High-Dielectric-Constant Perovskite-Related Oxide. *Science* **2001**, *293*, 673−676.
(22) Xiao, Z.; Zhou, Y.; Hosono, H.; Kamiya, T.; Padture, N. P. Bandgap Optimization of Perovskite Semiconductors for Photovoltaic Applications. *Chem.—Eur. J.* **2018**, *24*, 2305−2316.
(23) Meng, W.; Saparov, B.; Hong, F.; Wang, J.; Mitzi, D. B.; Yan, Y. Alloying and Defect Control within Chalcogenide Perovskites for Optimized Photovoltaic Application. *Chem. Mater.* **2016**, *28*, 821−829.
(24) Du, J.; Shi, J.-j. 2D $Ca_3Sn_2S_7$ Chalcogenide Perovskite: A Graphene-Like Semiconductor with Direct Bandgap 0.5 eV and Ultrahigh Carrier Mobility 6.710^4 cm^2 V^{-1} s^{-1}. *Adv. Mater.* **2019**, *31*, 1905643.
(25) Cen, Y.-l.; Shi, J.-j.; Zhang, M.; Wu, M.; Du, J.; Guo, W.-h.; Liu, S.-m.; Han, S.-p.; Zhu, Y.-h. Design of Lead-Free and Stable Two-Dimensional Dion-Jacobson-Type Chalcogenide Perovskite $A'La_2B_3S_{10}$ (A′ = Ba/Sr/Ca; B = Hf/Zr) with Optimal Band Gap, Strong Optical Absorption, and High Efficiency for Photovoltaics. *Chem. Mater.* **2020**, *32*, 2450−2460.
(26) Osei-Agyemang, E.; Adu, C. E.; Balasubramanian, G. Ultralow lattice thermal conductivity of chalcogenide perovskite $CaZrSe_3$ contributes to high thermoelectric figure of merit. *npj Computational Materials* **2019**, *5*, 116.
(27) Darriet, J.; Subramanian, M. A. Structural relationships between compounds based on the stacking of mixed layers related to hexagonal perovskite-type structures. *J. Mater. Chem.* **1995**, *5*, 543.
(28) Ball, J. M.; Petrozza, A. Defects in perovskite-halides and their effects in solar cells. *Nature Energy* **2016**, *1*, 16149.
(29) Stoumpos, C. C.; Cao, D. H.; Clark, D. J.; Young, J.; Rondinelli, J. M.; Jang, J. I.; Hupp, J. T.; Kanatzidis, M. G. Ruddlesden−Popper Hybrid Lead Iodide Perovskite 2D Homologous Semiconductors. *Chem. Mater.* **2016**, *28*, 2852−2867.
(30) Woodward, P. M. Octahedral Tilting in Perovskites. II. Structure Stabilizing Forces. *Acta Crystallographica Section B Structural Science* **1997**, *53*, 44−66.
(31) Xiao, Z.; Yan, Y. Progress in Theoretical Study of Metal Halide Perovskite Solar Cell Materials. *Adv. Energy Mater.* **2017**, *7*, 1701136.
(32) Yin, W. J.; Shi, T.; Yan, Y. Superior photovoltaic properties of lead halide perovskites: Insights from first-principles theory. *J. Phys. Chem. C* **2015**, *119*, 5253−5264.
(33) Katz, L.; Ward, R. Structure Relations in Mixed Metal Oxides. *Inorg. Chem.* **1964**, *3*, 205−211.
(34) Schüpp-Niewa, B.; Shlyk, L.; Prots, Y.; Niewa, R.; Krabbes, G. Crystal Structure of $Ba_3ZrRu_2O_9$ − a New 6H-$(cch)_2$ *Perovskite*. *Zeitschrift für anorganische und allgemeine Chemie* **2006**, *632*, 572−576.
(35) Deng, Z.; Kieslich, G.; Bristowe, P. D.; Cheetham, A. K.; Sun, S. Octahedral connectivity and its role in determining the phase stabilities and electronic structures of low-dimensional, perovskite-related iodoplumbates. *APL Materials* **2018**, *6*, 114202.
(36) Kamminga, M. E.; De Wijs, G. A.; Havenith, R. W.; Blake, G. R.; Palstra, T. T. The Role of Connectivity on Electronic Properties of Lead Iodide Perovskite-Derived Compounds. *Inorg. Chem.* **2017**, *56*, 8408−8414.
(37) Kamminga, M. E.; Fang, H.-H.; Filip, M. R.; Giustino, F.; Baas, J.; Blake, G. R.; Loi, M. A.; Palstra, T. T. M. Confinement Effects in Low-Dimensional Lead Iodide Perovskite Hybrids. *Chem. Mater.* **2016**, *28*, 4554−4562.
(38) Niu, S.; Zhao, H.; Zhou, Y.; Huyan, H.; Zhao, B.; Wu, J.; Cronin, S. B.; Wang, H.; Ravichandran, J. Mid-wave and Long-Wave Infrared Linear Dichroism in a Hexagonal Perovskite Chalcogenide. *Chem. Mater.* **2018**, *30*, 4897−4901.
(39) Fop, S.; McCombie, K. S.; Wildman, E. J.; Skakle, J. M. S.; Mclaughlin, A. C. Hexagonal perovskite derivatives: a new direction in the design of oxide ion conducting materials. *Chem. Commun.* **2019**, *55*, 2127−2137.
(40) Becker, P.; Márquez, J. A.; Just, J.; Al-Ashouri, A.; Hages, C.; Hempel, H.; Jošt, M.; Albrecht, S.; Frahm, R.; Unold, T. Low Temperature Synthesis of Stable γ-$CsPbI_3$ Perovskite Layers for Solar Cells Obtained by High Throughput Experimentation. *Adv. Energy Mater.* **2019**, *9*, 1900555.
(41) Wiegers, G. Misfit layer compounds: Structures and physical properties. *Prog. Solid State Chem.* **1996**, *24*, 1−139.
(42) Wiegers, G.; Meerschaut, A. Structures of misfit layer compounds $(MS)_nTS_2$ (M ≡ Sn, Pb, Bi, rare earth metals; T ≡ Nb, Ta, Ti, V, Cr; 1.08<*n*<1.23). *J. Alloys Compd.* **1992**, *178*, 351−368.
(43) Johnsson, M.; Lemmens, P., Crystallography and Chemistry of Perovskites In *Handbook of Magnetism and Advanced Magnetic Materials*; John Wiley & Sons, Ltd: Chichester, UK, 2007; Vol. *262*, pp 7486−7491.
(44) Li, W.; Wang, Z.; Deschler, F.; Gao, S.; Friend, R. H.; Cheetham, A. K. Chemically diverse and multifunctional hybrid organic−inorganic perovskites. *Nature Reviews Materials* **2017**, *2*, 16099.
(45) Chen, Y.; Sun, Y.; Peng, J.; Tang, J.; Zheng, K.; Liang, Z. 2D Ruddlesden−Popper Perovskites for Optoelectronics. *Adv. Mater.* **2018**, *30*, 1703487.
(46) Lelieveld, R.; IJdo, D. J. W. Sulphides with the $GdFeO_3$ structure. *Acta Crystallographica Section B Structural Crystallography and Crystal Chemistry* **1980**, *36*, 2223−2226.
(47) Clearfield, A. The synthesis and crystal structures of some alkaline earth titanium and zirconium sulfides. *Acta Crystallogr.* **1963**, *16*, 135−142.
(48) Perera, S.; Hui, H.; Zhao, C.; Xue, H.; Sun, F.; Deng, C.; Gross, N.; Milleville, C.; Xu, X.; Watson, D. F.; Weinstein, B.; Sun, Y. Y.; Zhang, S.; Zeng, H. Chalcogenide perovskites - an emerging class of ionic semiconductors. *Nano Energy* **2016**, *22*, 129−135.

https://doi.org/10.1021/acs.chemmater.2c01289
Chem. Mater. 2022, 34, 6894−6901

(49) Moroz, N. A.; Bauer, C.; Williams, L.; Olvera, A.; Casamento, J.; Page, A. A.; Bailey, T. P.; Weiland, A.; Stoyko, S. S.; Kioupakis, E.; Uher, C.; Aitken, J. A.; Poudeu, P. F. Insights on the Synthesis, Crystal and Electronic Structures, and Optical and Thermoelectric Properties of $Sr_{1-x}Sb_xHfSe_3$ Orthorhombic Perovskite. *Inorg. Chem.* **2018**, *57*, 7402−7411.
(50) Hanzawa, K.; Iimura, S.; Hiramatsu, H.; Hosono, H. Material Design of Green-Light-Emitting Semiconductors: Perovskite-Type Sulfide $SrHfS_3$. *J. Am. Chem. Soc.* **2019**, *141*, 5343−5349.
(51) Hahn, H.; Mutschke, U. Untersuchungen über ternäre Chalkogenide. XI. Versuche zur Darstellung von Thioperowskiten. *Zeitschrift für anorganische und allgemeine Chemie* **1957**, *288*, 269−278.
(52) Aslanov, L. A.; Kovba, L. M. Ternary sulphides of barium and tantalum, titanium, zirconium. *Russ. J. Inorg. Chem.* **1964**, *9*, 1317−1319.
(53) Aslanov, L. A. Selenides of the type $ABSe_3$. *Russ. J. Inorg. Chem.* **1964**, *9*, 1090−1091.
(54) Okai, B.; Takahashi, K.; Saeki, M.; Yoshimoto, J. Preparation and crystal structures of some complex sulphides at high pressures. *Mater. Res. Bull.* **1988**, *23*, 1575−1584.
(55) Ishii, M.; Saeki, M.; Sekita, M. Vibrational spectra of barium-zirconium sulfides. *Mater. Res. Bull.* **1993**, *28*, 493−500.
(56) Ishii, M.; Saeki, M. Raman and Infrared Spectra of $BaTiS_3$ and $BaNbS_3$. *physica status solidi (b)* **1992**, *170*, K49−K54.
(57) Onoda, M.; Saeki, M.; Yamamoto, A.; Kato, K. Structure refinement of the incommensurate composite crystal $Sr_{1.145}TiS_3$ through the Rietveld analysis process. *Acta Crystallographica Section B Structural Science* **1993**, *49*, 929−936.
(58) Saeki, M.; Onoda, M. Preparation of a New Strontium Titanium Sulfide Sr_xTiS_3 (x = 1.05 - 1.22) with Infinitely Adaptive Structures. *J. Solid State Chem.* **1993**, *102*, 100−105.
(59) Onoda, M.; Saeki, M. Rietveld analysis of an incommensurate composite crystal with a nominal composition $Sr_{1.19}TiS_3$. *Jpn. J. Appl. Phys.* **1993**, *32*, 752−753.
(60) Saeki, M.; Onoda, M. Preparation of a Chain-Type Composite Crystal, Ba_xTiS_3 (x = 1.00 - 1.05). *J. Solid State Chem.* **1994**, *112*, 65−69.
(61) Meetsma, A.; Wiegers, G. A.; de Boer, J. L. Structure determination of $SnZrS_3$. *Acta Crystallographica Section C Crystal Structure Communications* **1993**, *49*, 2060−2062.
(62) Lee, C. S.; Kleinke, K. M.; Kleinke, H. Synthesis, structure, and electronic and physical properties of the two $SrZrS_3$ modifications. *Solid State Sci.* **2005**, *7*, 1049−1054.
(63) Tranchitella, L. J.; Chen, B.-h.; Fettinger, J. C.; Eichhorn, B. W. Structural Evolutions in the $Sr_{1-x}Ba_xZrSe_3$ Series. *J. Solid State Chem.* **1997**, *130*, 20−27.
(64) Niu, S.; Huyan, H.; Liu, Y.; Yeung, M.; Ye, K.; Blankemeier, L.; Orvis, T.; Sarkar, D.; Singh, D. J.; Kapadia, R.; Ravichandran, J. Bandgap Control via Structural and Chemical Tuning of Transition Metal Perovskite Chalcogenides. *Adv. Mater.* **2017**, *29*, 1604733.
(65) Wei, X.; et al. Realization of $BaZrS_3$ chalcogenide perovskite thin films for optoelectronics. *Nano Energy* **2020**, *68*, 104317.
(66) Wang, Y.; Masuda, H.; Sato, N.; Yamada, K.; Fujino, T. Synthesis of Ba_xTiS_y in Sulfur Melt. *Shigen-to-Sozai* **1999**, *115*, 547−552.
(67) Wang, Y.; Sato, N.; Yamada, K.; Fujino, T. Effect of Halide Addition on the Syntheses of $PbTiS_3$ and Ba_xTiS_y in Sulfur Melt. *Shigen-to-Sozai* **2000**, *116*, 703−710.
(68) Wang, Y.; Sato, N.; Fujino, T. Synthesis of $BaZrS_3$ by short time reaction at lower temperatures. *J. Alloys Compd.* **2001**, *327*, 104−112.
(69) Tranchitella, L. J.; Fettinger, J. C.; Dorhout, P. K.; Van Calcar, P. M.; Eichhorn, B. W. Commensurate Columnar Composite Compounds: Synthesis and Structure of $Ba_{15}Zr_{14}Se_{42}$ and $Sr_{21}Ti_{19}Se_{57}$. *J. Am. Chem. Soc.* **1998**, *120*, 7639−7640.
(70) Wang, Y.; Sato, N.; Yamada, K.; Fujino, T. Synthesis of $BaZrS_3$ in the presence of excess sulfur. *J. Alloys Compd.* **2000**, *311*, 214−223.
(71) Chen, B.-H.; Eichhorn, B. Synthesis and structure of two new Ba_2MS_4 phases where M = Zr, Hf: A new series of K_2NiF_4 solids. *Mater. Res. Bull.* **1991**, *26*, 1035−1040.
(72) Chen, B. H.; Eichhorn, B. W.; Fanwick, P. E. Synthesis and structure of $Ba_6Hf_5S_{16}$ and $Ba_5Hf_4S_{13}$: the n = 5 and 4 members of the $A_{n+1}B_nX_{3n+1}$ Ruddlesden-Popper phases. *Inorg. Chem.* **1992**, *31*, 1788−1791.
(73) Chen, B. H.; Eichhorn, B.; Wong-Ng, W. Structural reinvestigation of $Ba_3Zr_2S_7$ by single-crystal X-ray diffraction. *Acta Crystallographica Section C Crystal Structure Communications* **1994**, *50*, 161−164.
(74) Sterzel, W. Darstellung und Eigenschaften von Bleithiotitanat. *Die Naturwissenschaften* **1966**, *53*, 199−199.
(75) Kniep, R.; Mootz, D.; Severin, U.; Wunderlich, H. Structure of tin(II) tin(IV) trisulphide, a redetermination. *Acta Crystallographica Section B Structural Crystallography and Crystal Chemistry* **1982**, *38*, 2022−2023.
(76) Mootz, D.; Puhl, H. Die Kristallstruktur von Sn_2S_3. *Acta Crystallogr.* **1967**, *23*, 471−476.
(77) Sterzel, W.; Horn, J. Thiotitanat, Thiozirkonat und Thiohafnat des Bleis mit der Zusammensetzung $PbMe^{IV}S_3$. *Zeitschrift für anorganische und allgemeine Chemie* **1970**, *376*, 254−260.
(78) Schmidt, L. Superconductivity in $PbNbS_3$ and $PbTaS_3$. *Phys. Lett. A* **1970**, *31*, 551−552.
(79) Jumas, J.-c.; Ribes, M.; Philippot, M. M. Sur le systeme SnS_2-PbS. Structure cristalline de $PbSnS_3$. *C. R. Acad. Sc. Paris Serie C* **1972**, *275*, 269−271.
(80) Yamaoka, S. Synthesis of $PbZrS_3$ at High Pressures. *J. Am. Ceram. Soc.* **1972**, *55*, 111−111.
(81) Lelieveld, R.; Ijdo, D. J. W. Lead zirconium sulphide. *Acta Crystallographica Section B Structural Crystallography and Crystal Chemistry* **1978**, *34*, 3348−3349.
(82) Wiegers, G. A.; Meetsma, A.; Haange, R. J.; de Boer, J. L. Structure of tin hafnium sulfide and lead hafnium sulfide. *Acta Crystallographica Section C Crystal Structure Communications* **1989**, *45*, 847−849.
(83) Van Maaren, M. H. Superconductivity in tin -group V^a trichalcogenides. *Phys. Lett. A* **1972**, *40*, 353−354.
(84) Harada, D.; Richard, A.; Zakutayev, A.; Keszler, D.; Tate, J., Optical and Transport Properties of $SnZrCh_3$ (Ch = S, Se). Presented at *APS March Meeting 2010*, Portland, Oregon, March 15−19, 2010; Abstract no. S1.00228. See the following: https://meetings.aps.org/Meeting/MAR10/Event/119517.
(85) Gardner, R. A.; Vlasse, M.; Wold, A. Electrical properties and crystal structure of barium tantalum sulfide, $BaTaS_3$. *Inorg. Chem.* **1969**, *8*, 2784−2787.
(86) Gardner, R. A.; Vlasse, M.; Wold, A. Preparation, properties and crystal structure of barium vanadium sulfide, $BaVS_3$. *Acta Crystallographica Section B Structural Crystallography and Crystal Chemistry* **1969**, *25*, 781−787.
(87) Donohue, P.; Weiher, J. The preparation and properties of $BaTa_{0.8}S_3$, $BaNb_{0.8}S_3$, and $BaTa_{0.8}Se_3$. *J. Solid State Chem.* **1974**, *10*, 142−144.
(88) Mar, A.; Ibers, J. A. Structure of europium zirconium selenide, $EuZrSe_3$. *Acta Crystallographica Section C Crystal Structure Communications* **1992**, *48*, 771−773.
(89) Sunshine, S. A.; Ibers, J. A. Redetermination of the structures of $CuTaS_3$ and Nb_2Se_9. *Acta Crystallographica Section C Crystal Structure Communications* **1987**, *43*, 1019−1022.
(90) Narducci, A. A.; Ibers, J. A. Ternary and Quaternary Uranium and Thorium Chalcogenides. *Chem. Mater.* **1998**, *10*, 2811−2823.
(91) Ward, M. D.; Ibers, J. A. Nickel(II) uranium(IV) trisulfide. *Acta Crystallographica Section E Structure Reports Online* **2014**, *70*, i4−i4.
(92) Brochu, R.; Padiou, J.; Grandjean, D. Preparation et structure cristalline du sulfure dauranium et de baryum: $BaUS_3$. *C. R. Acad. Sc. Paris Serie C* **1970**, *274*, 642−643.
(93) Prakash, J.; Tarasenko, M. S.; Mesbah, A.; Lebègue, S.; Malliakas, C. D.; Ibers, J. A. Synthesis, Crystal Structure, Theoretical, and Resistivity Study of $BaUSe_3$. *Inorg. Chem.* **2016**, *55*, 7734−7738.

https://doi.org/10.1021/acs.chemmater.2c01289
Chem. Mater. 2022, 34, 6894−6901

(94) Yamaoka, S.; Okai, B. Preparations of $BaSnS_3$, $SrSnS_3$ and $PbSnS_3$ at high pressure. *Mater. Res. Bull.* **1970**, *5*, 789−794.
(95) Nishigaki, Y.; Nagai, T.; Nishiwaki, M.; Aizawa, T.; Kozawa, M.; Hanzawa, K.; Kato, Y.; Sai, H.; Hiramatsu, H.; Hosono, H.; Fujiwara, H. Extraordinary Strong Band-Edge Absorption in Distorted Chalcogenide Perovskites. *Solar RRL* **2020**, *4*, 1900555.
(96) Kuhar, K.; Crovetto, A.; Pandey, M.; Thygesen, K. S.; Seger, B.; Vesborg, P. C. K.; Hansen, O.; Chorkendorff, I.; Jacobsen, K. W. Sulfide perovskites for solar energy conversion applications: computational screening and synthesis of the selected compound $LaYS_3$. *Energy Environ. Sci.* **2017**, *10*, 2579−2593.
(97) Goldschmidt, V. M. Die Gesetze der Krystallochemie. *Die Naturwissenschaften* **1926**, *14*, 477−485.
(98) Shannon, R. D. Revised effective ionic radii and systematic studies of interatomic distances in halides and chalcogenides. *Acta Crystallogr., Sect. A* **1976**, *32*, 751−767.
(99) Bartel, C. J.; Sutton, C.; Goldsmith, B. R.; Ouyang, R.; Musgrave, C. B.; Ghiringhelli, L. M.; Scheffler, M. New tolerance factor to predict the stability of perovskite oxides and halides. *Science Advances* **2019**, *5*, eaav0693.
(100) Xie, S. R.; Kotlarz, P.; Hennig, R. G.; Nino, J. C. Machine learning of octahedral tilting in oxide perovskites by symbolic classification with compressed sensing. *Comput. Mater. Sci.* **2020**, *180*, 109690.
(101) Pearson, W. Relative atomic size in semiconductor chemistry. *J. Phys. Chem. Solids* **1962**, *23*, 103−108.
(102) Brehm, J. A.; Bennett, J. W.; Schoenberg, M. R.; Grinberg, I.; Rappe, A. M. The structural diversity of ABS_3 compounds with d^0 electronic configuration for the B-cation. *J. Chem. Phys.* **2014**, *140*, 224703.
(103) Travis, W.; Glover, E. N. K.; Bronstein, H.; Scanlon, D. O.; Palgrave, R. G. On the application of the tolerance factor to inorganic and hybrid halide perovskites: a revised system. *Chemical Science* **2016**, *7*, 4548−4556.
(104) Pettifor, D. A chemical scale for crystal-structure maps. *Solid State Commun.* **1984**, *51*, 31−34.

https://doi.org/10.1021/acs.chemmater.2c01289
Chem. Mater. 2022, 34, 6894−6901